Structural Analysis of a Filamentous Chaperonin from *Sulfolobus solfataricus*

Yi C. Zeng[1], Meghna Sobti[1,2], and Alastair G. Stewart[1,2]

[1]Molecular, Structural and Computational Biology Division, The Victor Chang Cardiac Research Institute, Darlinghurst, Australia

[2]Faculty of Medicine, The University of New South Wales, Sydney, Australia

*For correspondence: a.stewart@victorchang.edu.au

SUMMARY/Abstract

Chaperonins are biomolecular complexes that assist protein folding. Thermophilic Factor 55 (TF55) is a group II chaperonin found in the archaeal genus *Sulfolobus* and which undergoes changes in modular subunit composition in a temperature-dependent manner. TF55 can form filamentous assemblies that may be a component of the archaeal cytoskeleton or sequester inactive chaperonin. Using cryo-electron microscopy, we have determined the structure of the β-only complex of *S. solfataricus* TF55 complexes to 3.6 Å resolution and its filamentous form to 5.2 Å resolution. Filament formation can be induced when the protein is enriched in solution or in the presence of the detergent dodecyl maltoside. Helical protrusions in the apical domain facilitate end-on-end interactions in the filamentous state. Our findings establish the molecular basis for forming chaperonin filaments in *Sulfolobus* and may suggest how filament formation could function as a cold-shock response and provides a background for generating tuneable protein nanowires.

Keywords

chaperonin; filaments; cryo-EM

INTRODUCTION/Main

Chaperonins are large protein complexes that aid in both protein folding and in preventing aggregate-formation by misfolded proteins (Lopez et al., 2015; Saibil, 2013; Skjærven et al., 2015). Chaperonins are typically up-regulated during cellular stress or heat-shock to form large (~1 MDa) molecular cages. These molecular cages are constructed from one or more types of subunit and can capture misfolded protein substrates into their inner cavity. Refolding of the misfolded substrate is achieved by the chaperonin closing around it, which perturbs the local energy minima of the substrate. The energy is provided by adenosine triphosphate (ATP) binding and hydrolysis. Group I chaperonins, such as GroEL that is found in eubacteria, form tetradecamers of end-to-end stacked heptameric rings and require heptameric co-chaperones (termed GroES) to close and mediate refolding of the captured protein (Skjærven et al., 2015; Weiss et al., 2016). Group II chaperonins, such as TRiC/CCT that is found in eukaryotes, or TF55 that is found in archaea, are similarly composed of two multimeric stacked rings, but do not require a co-chaperone. The functional and substrate specificity of these chaperonins is mediated by their subunit composition and geometry that work together in a highly cooperative manner (Bigotti and Clarke, 2008; Lopez et al., 2015; Skjærven et al., 2015).

Thermophilic Factor 55 (TF55/rosettasome) is a chaperonin found in *Sulfolobus*, a genus of archaea typically residing in volcanic springs at pH 2–3 with temperatures around 75–

80°C (Quehenberger et al., 2017; Trent et al., 1991). As a result of the harsh environment in which it lives, the TF55 chaperonin is crucial for the survival of these archaea. Moreover, TF55 implements different means of chaperonin regulation and function. Under different conditions, the proportion of its α, β, and γ subunits that are present can differ. At temperatures above 80 °C, TF55 is expressed at high levels in *Sulfolobus* due to the presence of a heat-inducible promoter for the *tf55* gene (Jonuscheit et al., 2003; Trent et al., 1990). However, the subunit composition and geometry of the chaperonin is regulated in a temperature-dependent manner, altering between $\alpha_6\beta_6\gamma_6$, $\alpha_8\beta_8$, or β_{18} complexes as temperature increases, respectively (Chaston et al., 2016; Kagawa et al., 2003). In addition, filaments of TF55 chaperonin have been observed in *S. shibatae*, which have been suggested to be a component of the archaeal cytoskeleton (Trent et al., 1997). Functionally, the formation of chaperonin-based filaments might serve to sequester the inactive complex until required, where it would dissociate and be liberated to aid in protein refolding (Trent et al., 1998). Moreover, the ability of TF55 chaperonin to self-assemble into filaments and, in the case of synthetic mutants, 2D ordered structures, has the potential to be exploited in the nanobiotechnology field to generate protein nanowires and nanostructures (Li et al., 2007; Whitelam et al., 2009).

To investigate the filament assembly of chaperonins, we performed cryo-electron microscopy (cryo-EM) on TF55 composed of only the β subunit (TF55β) from the thermophilic archaea *S. solfataricus*. Filaments of TF55β can be observed at high concentrations (> 10 mg mL^{-1}) or can be induced by the addition of dodecyl maltoside (DDM) at low temperatures. We have determined the structure of isolated TF55β complexes to 3.6 Å resolution together with the structure of filamentous TF55β to 5.2 Å resolution. These objects resemble respectively the biological unit and crystal lattice contacts of the TF55β crystal structure determined previously (Chaston et al., 2016). These new structural data together with previous work on related TF55

structures suggest that the filamentous architecture seen in *S. shibatae* may be common to archaea of *Sulfolobus*. These could potentially function as a cold-shock response to sequester unengaged chaperonin, whereas at higher temperatures, heat dissociation would then liberate the TF55β complex from the filament, allowing it to function effectively as a molecular chaperone. These structures also provided crucial background information needed for the generation of tuneable protein nanowires.

RESULTS

Single particle analysis of the TF55β complex

Cryo-EM images of dispersed TF55β chaperonin at 20 mg/ml (Figure 1A) generated an initial 145,924 particles picked automatically in RELION (Zivanov et al., 2018) and subsequent 2D and 3D classification yielded 37,592 particles that contributed to the final model (Figure 1B). The images showed a high proportion of top views, characterized by a nonameric ring (the octadecameric β complex), and side views were more difficult to observe due to their lower contrast and abundance (Figure 1A). Our reconstruction showed the octadecameric complex in its open configuration (Figure 1C, 1D). 3D refinement was performed with either C_1 or D_9 symmetry imposed and resulted in final estimated resolutions of 4.4 Å and 3.6 Å, respectively (Figure S1C). Sidechain density for the equatorial and intermediate domain was more evident in the D_9 symmetric map, whereas the β-sheets of the intermediate domain were more visible in the C_1 symmetric model (Figure S1D). There was generally excellent model-to-density correlation between the crystal structure and the equatorial domain of the cryo-EM map (average root mean square deviation [RMSD] per subunit was 1.1 Å, Figure S1E), however, clearer density for the loop regions were observed in the cryo-EM map. Because the map density was weak for the intermediate and apical domains these were modelled using

rigid-body docking followed by molecular dynamics flexible fitting (MDFF). Non-crystallographic symmetry (NCS)-averaging of the C_1 map aided rigid-body fitting against the β-sheets in the apical domain which was then equilibrated and minimised through MDFF.

The model of TF55β obtained by cryo-EM shows the chaperonin in its open conformation. The apical domain is hinged at the helices of the intermediate domain and this generates an outwards tilt relative to the conformation seen in the crystal structure (Chaston et al. 2016), with an overall RMSD of 2.1 Å across each subunit (Figure S1E). Our cryo-EM model more likely reflects the structure of the chaperonin in solution, with no crystal contacts between complexes that could induce crystal packing artefacts. The highly flexible apical domain plays a key role in the opening/closing of the complex and a similar feature is conserved throughout chaperonins in other organisms (Chaudhry et al., 2004; Zang et al., 2016). The stem loop in the apical domain forms an extended β-sheet with the terminal β-strands of the adjacent subunit near the nucleotide binding site (Figure S1F). Map density for the nucleotide binding site indicated that the ligand bound was ATP (Figure S1G) rather than the ADP seen in the crystal structure (Chaston et al. 2016), with multiple residues coordinating to the ribose sugar and phosphates. The magnesium ion was coordinated to the phosphates of ATP and also to Asp101, at the base of the stem loop. There was also a large open pocket that may be occupied by water molecules coordinated to nearby polar residues (Figure S1G). The lower resolution achieved in the intermediate and apical domains may indicate that these regions are more dynamic in solution. In particular, the lack of density for the helical protrusion may suggest that this secondary structure could be prone to unfolding as seen in the crystal structure of the TF55αβ hexadecameric complex (Chaston et al., 2016).

TF55β filaments form at high protein concentrations, but are disassembled by EDTA

At concentrations of 9 mg/ml, short assemblies of TF55β could be observed on grids, and were localised preferentially near the edge of the holes of the holey carbon grid (Figure 2A). When concentrated to 20 mg/ml (the concentration used for single particle analysis), longer filaments could be observed alongside top views of the TF55β complex (Figure 2B). However, initial attempts to analyse these filaments were hindered by the single particles, which interfered with helical reconstruction. The addition of EDTA in excess of magnesium ion concentration present, caused the filaments to dissociate (Figure 2C) as previously observed in *S. shibatae* TF55 (Trent et al., 1997), but also visibly reduced the number of TF55β complexes. EDTA is able to release nucleotides from chaperonin complexes (Lin et al., 2013) and, because ATP is required for the monomeric TF55β to assemble into TF55β complex, this particular chaperonin may be unstable without the presence of both Mg^{2+} and ATP (Trent et al., 1997).

Filamentous TF55β assembly can be induced by DDM

While attempting to overcome the preferential orientation problem common to cryo-EM of group II chaperonins (Zang et al., 2016), we found serendipitously that the inclusion of 0.005% DDM could cause the TF55β complex to form long filamentous assemblies without any trace of single particles (Figure 2D), even at a lower concentration of 10 mg/ml. Thermal melt analysis of the chaperonin in the presence of different concentrations of DDM (Figure 2E) appeared to suggest that filament formation was partially dependent on detergent concentration, analogous to that noted previously for SDS in the GroEL system (Chen et al., 2015). The filaments of TF55β generated with DDM resembled those previously described in *S. shibatae* (Trent et al., 1997) and showed characteristic striations both at the nonameric double ring of

individual TF55β complexes and at the contacts between end-to-end stacked chaperonin. 2D class averaging of a two-chaperonin segment produced a striking similarity to a 2D projection of the crystal structure lattice (Figure 2F).

Using a single-particle analysis approach in the cryoSPARC2 workflow (Punjani et al., 2017), a two-chaperonin segment of the filament could be refined to a resolution of 5.2 Å (Figure 3A, S3). Density for the intermediate and apical domains was much clearer than that seen with the chaperonin in isolation, probably as a result of the contacts between the apical domains rigidifying this area. Akin to the crystal lattice contacts, the protruding helix overlaps with the helix of the adjacent unit, locking each other along the filament (Figure 3B). In the crystal structure, the protruding helices crossed towards the centre of the helix. However, MDFF fitting of the cryo-EM model in ISOLDE (Croll, 2018) and NAMD (Trabuco et al., 2008) together with secondary structure restraints minimised on an interaction at the distal end of the helix.

DISCUSSION

The current cryo-EM structure of the TF55β chaperonin complex from *S. solfataricus* shows many structural similarities with chaperonins from other organisms. Comparisons with the crystallized TF55β complex demonstrated a mobile stem loop that changed between ATP-bound (open, before misfolded substrate binding) and ADP-bound (after hydrolysis and substrate release) states, similar to the changes observed in crystal structures of open- and closed-state of the group I chaperonin GroEL (Saibil et al., 2013) and a group II-like chaperonin from the bacteria *Carboxydothermus hydrogenoformans* (An et al., 2017). The stem loop that forms β-sheets with the N- and C-terminus of the neighbouring subunit may allosterically

coordinate ring closing through contacts at the base of the loop with the nucleotide together with conformational changes generated by the binding of a misfolded substrate protein at the equatorial-intermediate domains, as seen in the eukaryotic CCT:tubulin-bound complex (Muñoz et al., 2011; Saibil et al., 2013).

The apical domain in the two cryo-EM structures presented here demonstrated its flexibility and indicated how it functions in protein recognition. The flexibility of the protruding helix in the open conformation of TF55β, as implied by a lack of density and resolution in this area, is recapitulated in the ability of this secondary structure to partially unwind in the α subunit of the TF55αβ crystal structure, where it forms a β-strand that binds inside the equatorial hydrophobic pocket of the neighbouring crystal lattice subunit (Chaston et al., 2016). The inherent flexibility or disorder of this element of the structure together with that the accompanying loop in solution, may be crucial for the recognition of misfolded protein substrates entering the chaperonin (Skjærven et al., 2015). In the filamentous form, the protruding helices appear to be able to recognise and contact successive chaperonin complexes, forming a locked tubular filament. Although 2D projections of the crystal lattice of TF55β are almost identical to the 2D averaged cryo-EM filament, modelling into the cryo-EM map suggests that the interacting surface may slightly differ between the solid and solution states. Nonetheless, the filamentous structure, in combination with our thermal melt assay, provides insight into the possible role of this assembly in archaea. Unlike *S. shibatae,* TF55β from *S. solfataricus* required much higher concentrations to assemble into filaments *in vitro,* despite their sharing 98% sequence identity in the β subunit, although this difference may result from other factors such as ion or ATP concentrations (Kagawa et al., 2003). Our thermal melt analysis, which shows a slow transition between 20 to 60 °C, suggests that these filaments are not stable at the higher temperatures *Sulfolobus* are normally found and are unlikely to be a

component of the archaeal cytoskeleton. The concentrations of magnesium in the work of (Trent et al., 1997) was ten times higher than that normally found inside a cell and may account for the observed filaments at chaperonin concentrations of 1 mg/ml. We propose that the filamentation of TF55β could be a cold-shock response that functions to sequester unengaged chaperonin (Trent et al., 1998). At higher temperatures, heat dissociation would then liberate the TF55β complex from the filament, allowing it to function effectively as a molecular chaperone (Figure 4). Interestingly, filament assembly of chaperonins has also been observed in thermophilic bacterium in which similar morphologies appear to be present, suggesting possible evolutionary conservation for thermophiles (Furutani et al., 1998), although further work will be required to evaluate fully this function *in vitro* and also the influence of ions or nucleotide concentration on filament formation.

Mutants of *S. shibatae* TF55β have been examined for their ability to form both filaments as well as monolayers, providing potentially useful materials or coatings for biotechnological applications (Li et al., 2007). Surprisingly, removing segments of the protruding helix or the apical domain of TF55β from *S. shibatae* created mutants that were still able to form filaments, possibly suggesting that the overall architecture, and not purely the helical protrusion, is capable of assembly into filamentous forms.

The ability of TF55β to form filaments in the presence of DDM also has implications for the production of switchable nanowires. As demonstrated for both TF55β and GroEL, detergents can induce filament formation and could be used to control the filamentation process (Chen et al., 2015). NMR studies showed that SDS binds to the inner hydrophobic pocket in their apical domain, which is a known polypeptide substrate-binding site (Saibil et al., 2013).

Our thermal melt assay showed that detergent concentration was critical in the formation of filaments TF55β analogous to that seen with GroEL (Chen et al., 2015). High submicellar concentrations of detergent were required to form detectable and long filaments at lower protein concentrations. TF55β filaments could similarly be disassembled either through dilution (Furutani et al., 1998) or through addition of excess EDTA to release nucleotides and magnesium. Alternatively, as demonstrated for the GroEL-SDS system, cysteine mutants could be designed to rigidify the filament through disulfide bond formation, so that they could also be disassembled using a reducing agent (Chen et al., 2015). Our cryo-EM structures of filamentous TF55β highlights the potential interacting surface at the protruding helix during filament assembly and so provides crucial background information needed for the generation of tuneable protein nanowires.

Acknowledgments

We wish to thank and acknowledge Jen Coombs (formerly at the School of Biochemistry, University of Bristol) who aided in the initial analysis of this project. We would also like to thank Dr. James Walshe (Victor Chang Cardiac Research Institute) who provided assistance with model building. A.G.S was supported by a National Health and Medical Research Council Fellowship APP1159347 and Grant APP1146403. We wish to thank and acknowledge the use of the Victor Chang Cardiac Research Institute Innovation Centre, funded by the NSW Government, and the Electron Microscope Unit at UNSW Sydney, funded in part by the NSW Government.

Author Contributions

A.G.S. and Y.C.Z. conceived the study and wrote the manuscript. A.G.S. supervised the study. Y.C.Z. performed the formal analysis of the study (purified protein, prepared cryo-EM grids, performed reconstructions). M.S. took the cryo-EM dataset and edited the manuscript.

Declaration of Interests

Competing interests: Authors declare no competing interests

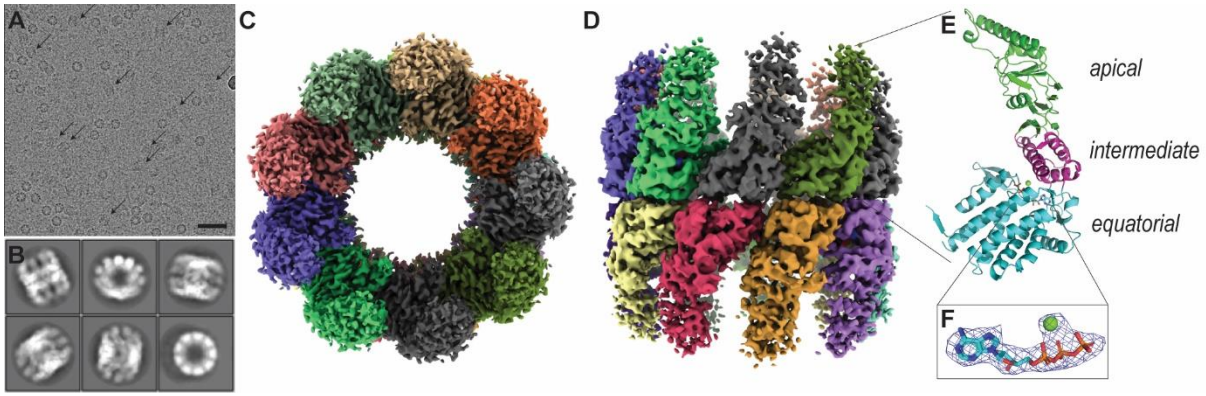

Figure 1: The cryo-EM structure of the octadecameric TF55β complex. (A) Representative cryomicrograph of TF55β chaperonins. Arrows pointed at side and tilted views of the complex. Scale bar are 50 nm. (B) Selected 2D class averages of TF55β chaperonin from particles contributing to the final 3D reconstruction map. (C, D) Cryo-EM map of TF55β chaperonin viewed from the top (C) and side (D), with colours segmenting each corresponding subunit of the homo-octadecamer. (E) Cartoon representation of a subunit of the TF55β complex, with the domains coloured and labelled (apical, green; intermediate, purple; equatorial, cyan). (F) Cryo-EM density (blue mesh) around Mg•ATP (sphere and stick model) within the binding site of a subunit of the TF55β complex. Map density contoured at 4 σ.

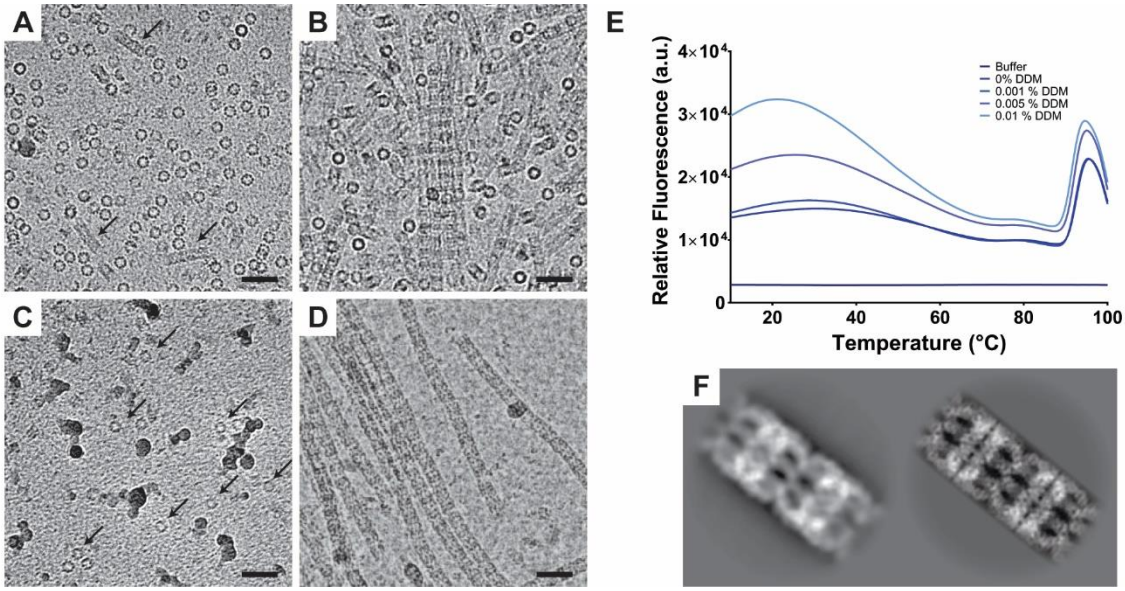

Figure 2: TF55β filament formation. (A–D) Micrographs of TF55β chaperonin under different conditions near the edge of the grid holes. Scale bars are 50 nm. (A) TF55β at 9 mg/ml, arrows pointed at small assemblies of chaperonins. (B) TF55β at 20 mg/ml, showing striated filaments and top views of single complexes (rings). (C) TF55β at 19 mg/ml and 5 mM EDTA, showing loss of filaments to single complexes (arrow, ring particles). (D) TF55β at 9 mg/ml and 0.005% DDM, showing striated filaments only. (E) Thermal melt analysis of TF55β at 1 mg/ml, with increasing fluorescence with higher DDM concentration (decreasing colour intensity). Solvent blank in darkest blue. Additional conditions and controls are included in Figure S2. (F) 2D class average of a segment of the filamentous TF55β (left) and a 2D projection from the crystal lattice of TF55β (right, PDB ID: 4XCD) showing striking similarities in the mode of interaction between complexes.

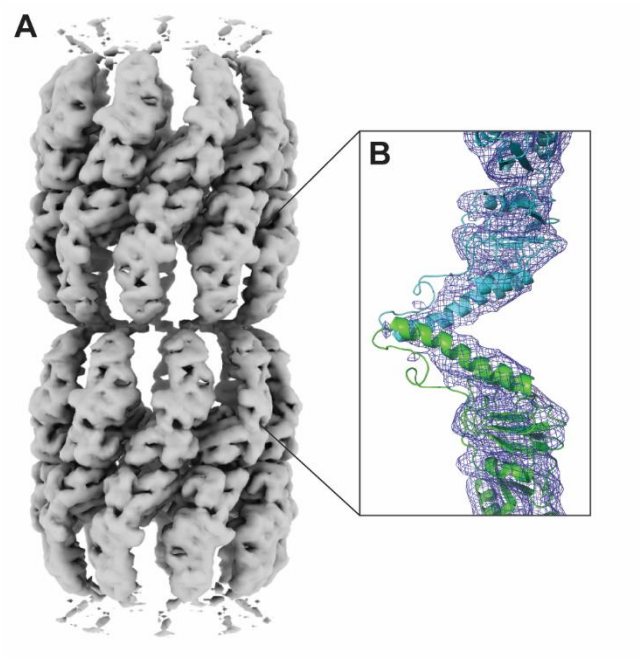

Figure 3: Cryo-EM structure of filamentous TF55β. (A) Cryo-EM map of a two-chaperonin segment of the filamentous TF55β. (B) MDFF of two subunits from the isolated complex model (cartoon) into the cryo-EM map (blue mesh) reveals an interaction near the apex of the helical protrusion.

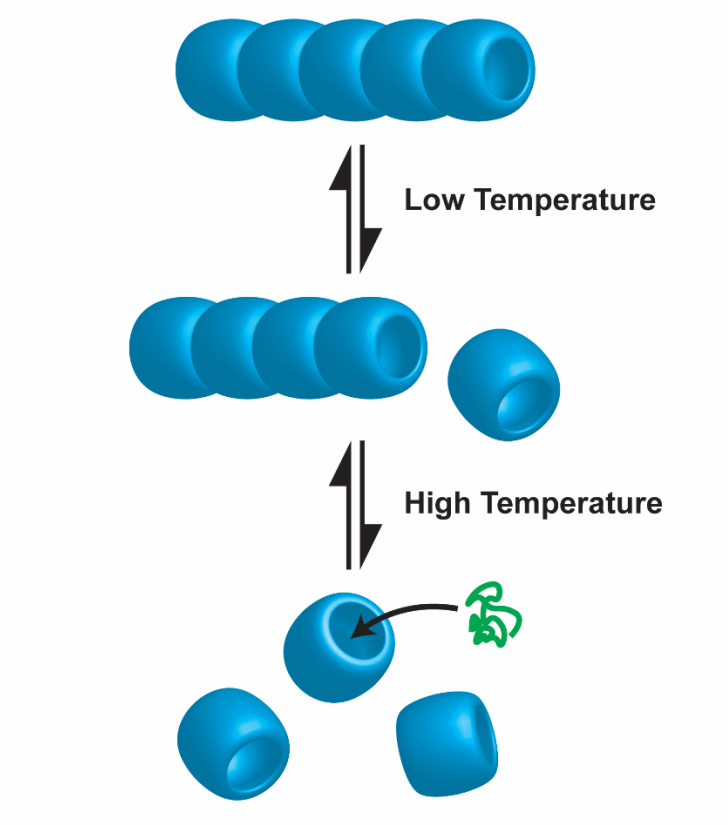

Figure 4: Proposed mechanism for filamentation in response to temperature-shock. At low temperatures (< 30 °C) and sufficient concentrations, TF55β complexes assembles (hollow blue cylinders) into filaments, while increasing temperatures up to 60 °C sees dissociation of the complex from the filament, resulting in liberated chaperonin at the high temperatures typically seen for *Sulfolobus* that can then aid refolding of misfolded proteins (green).

MATERIALS AND METHODS

Purification of TF55β complex from *S. solfataricus*

The TF55β complex was purified from *S. solfataricus* as described previously (Chaston et al., 2016). *S. solfataricus* (DSM1617) cell paste was purchased from the University of Georgia Biofermentation Facility. Cells were grown at 80 °C (pH 3.7) and harvested at an OD_{600} of 1.2. 20 g of cell paste was resuspended in 350 mL of lysis buffer (50 mM Tris/Cl pH

8.0, 5 mM $MgCl_2$, 0.001% PMSF, 100 mM NaCl, 1% DDM) and sonicated using a Branson Digital Sonifier for 3 min at 30 % amplitude with 1 s on/off cycles. The lysate was centrifuged in a Beckman 45Ti rotor at 100,000 x g for 30 min at 4 °C and the supernatant was applied to a HiLoad 26/10 Q Sepharose column (GE Life Sciences) equilibrated in 90 % buffer A and 10% buffer B (buffer A: 20 mM Tris/Cl pH 8.0, 2 mM $MgCl_2$, 1 mM EDTA, 0.001% PMSF, 0.05% DDM; buffer B: same as A with 1 M NaCl). The column was washed until baseline was achieved and the protein was eluted in a 10-50% buffer B gradient over 400 mL. Fractions containing TF55 were pooled and concentrated to less than 10 mL before applying to a HiPrep 16/60 Sephacryl S-300 column equilibrated in buffer C (20 mM Tris/Cl pH 8.0, 2 mM MgCl2, 1 mM EDTA, 100 mM NaCl). Fractions corresponding to the β subunit of TF55 (as assessed by mass spectrometry finger printing) were pooled and Mg•ATP was added to a final concentration of 2 mM. This sample was then concentrated to 0.5 mL and applied to a Superose 6 10/300 GL column equilibrated in buffer C (20 mM Tris/Cl pH 8.0, 2 mM $MgCl_2$, 1 mM EDTA, 100 mM NaCl) to obtain the TF55β complex (Figure S1A, S1B). The protein was concentrated to 20.0 mg mL^{-1}, which was then flash frozen and stored at –80 °C before use.

Cryo-EM grid preparation, data collection, and data processing for single particle TF55β complex

A 3.5 µL droplet of purified TF55β complex was applied on a copper grid with holey carbon film (Quantifoil Copper R1.2/1.3, 200 mesh) that had been glow discharged for 60 s. Grids were blotted for 5 s and flash-frozen in liquid ethane using a FEI Vitrobot Mark IV.

Grids were transferred to a FEI Talos Arctica transmission electron microscope operating at 200 kV. Images were recorded automatically using EPU at a magnification of

150,000 ×, yielding a pixel size of 0.986 Å. A dose rate of 50 electrons (spread over 29 frames) per $Å^2$ per second and a total exposure time of 61 s were used on the Falcon-III detector operating in counting mode. 1641 movies were collected in total.

The data processing workflow for single particle analysis is summarised in Figure S1D. In brief, MotionCor2 (Zheng et al., 2017) was used to correct local beam-induced motion and to align resulting frames using 5 × 5 patches. Defocus and astigmatism values were estimated using CTFFIND4 (Rohou and Grigorieff, 2015), and 14 micrographs were excluded due to drift or excessive ice contamination. All further data processing was performed in RELION 3 (Zivanov et al., 2018). The main challenge in auto-picking lay in the difficulty of picking side views of the complex which were less populated and harder to distinguish compared to the top views. Ultimately this was only afforded after using manually picked top and side views as initial templates for auto-picking a subset of micrographs which then, using the 16 Å resolution map of TF55 $\alpha_6\beta_6\gamma_6$ chaperonin (EMD-6291) low-pass filtered to 30 Å as the reference model for 3D classification, afforded a 3D template that succeeded in picking both top and side views of the complex. After two rounds of 2D and 3D classification, the model was refined using the 3D auto-refinement module imposed with D_9 symmetry. Further 3D auto-refinement was performed after particle polishing and CTF refinement in RELION. The final resolution of the complex was estimated to be 3.6 Å based on the gold-standard Fourier Shell Correlation (FSC = 0.143) criterion (Figure S1C). The same procedure was used to process the TF55β chaperonin map with C_1 symmetry, yielding an estimated resolution of 4.4 Å based on the gold-standard Fourier Shell Correlation (FSC = 0.143) criterion (Figure S1C).

Initially, chain A of the crystal structure of TF55β (PDB ID: 4XCD, Chaston et al., 2016) was docked as a rigid body into the density of one of the subunits in the D_9 symmetric cryo-EM map using Chimera's fitting program (Pintilie et al., 2010). Due to weak density in the apical domain of the complex, the equatorial and intermediate domains (residues 21–202, 382–531) were modelled independently using Coot (Emsley et al., 2010), Phenix real-space refinement (Adams et al., 2010), and ISOLDE (Croll, 2018). Rigid body fitting of the apical domain (residues 203-381) was performed in Coot before molecular dynamics flexible fitting (MDFF) in ISOLDE, aided by the non-crystallographic symmetry (NCS)-averaged map generated in Coot from the map solved with C_1 symmetry. Figures were prepared using PyMOL (Schrodinger, LLC), Chimera (Pettersen et al., 2004) or ChimeraX (Goddard et al., 2018).

Cryo-EM grid preparation, data collection, and data processing for filamentous TF55β

TF55β chaperonin was diluted with buffer C containing 0.01% DDM to obtain a final protein concentration of 10 mg/ml and DDM concentration of 0.005%, incubating on ice for 30 min. A 3.5 µL droplet of the sample was applied on a copper grid with holey carbon film (Quantifoil Copper R1.2/1.3, 200 mesh) that had been glow discharged for 60 s. Grids were blotted for 4 s and flash-frozen in liquid ethane using a FEI Vitrobot Mark IV.

Grids were transferred to a FEI Talos Arctica transmission electron microscope operating at 200 kV. Images were recorded automatically using EPU at a magnification of 92,000 ×, yielding a pixel size of 1.6 Å. A dose rate of 30 electrons (spread over 30 frames) per $Å^2$ per second and a total exposure time of 116 s were used on the Falcon-III detector operating in counting mode. 436 movies were collected in total.

The data processing workflow for the TF55β filament is summarised in Figure S3. Micrographs were imported into cryoSPARC2 (Punjani et al., 2017) and motion correction and CTF estimation were performed using the Patch motion or Patch CTF programs respectively. 29 micrographs were discarded on the basis of drift or excessive ice contamination. From a 2D template of filaments that were manually traced using e2helixboxer.py (Tang et al., 2007) and 2D classified, segments of filaments were automatically picked in cryoSPARC2 using the template picker to obtain 36,108 segments from 406 micrographs. After two rounds of 2D classification to filter out junk particles and bad segments, a final 32,363 segments with a box size of 300 pixels were then subjected to *ab initio* reconstruction with D_9 symmetry applied in order to obtain a segment with two full chaperonins. Further homogenous and non-uniform refinement after re-extracting particles from local motion correction converged on a map with an estimated resolution of 5.2 Å based on the gold-standard Fourier Shell Correlation (FSC = 0.143) criterion. Docking and manual fitting was initially performed in ChimeraX/ISOLDE using two chains of the cryo-EM model of TF55β chaperonin orientated at the helical protrusion interface. The resulting coordinates were used as the starting model for further MDFF in NAMD (Trabuco et al., 2008). Figures were prepared using PyMOL, Chimera or ChimeraX.

Thermal melting assay

Changes in the protein structure upon heating were monitored by SYPRO orange, a dye that fluoresces when bound to hydrophobic patches of the protein as it denatures. Fluorescence was measured in triplicate on the CFX384 Touch Real-Time PCR Detection System (Bio-Rad) in FRET mode over a temperature gradient of 10 to 100 °C. Each 20 µL reaction contained

SYPRO orange (15×) and a combination of 0, 0.1, or 1.0 mg/ml of purified TF55β with 0, 0.001, 0.005, or 0.01% DDM in buffer C.

Data and Code Availability

The accession number for the deposited coordinates of the TF55β chaperonin complex reported in this paper is PDB ID: 6VIC. The accession numbers for the TF55β chaperonin complex and filament cryo-EM maps are EMDB: EMD-21209 (D_9 symmetric refinement), EMD-21210 (C_1 symmetric refinement), and EMD-21211 (two-chaperonin segment of filamentous TF55β).

References

Adams, P.D., Afonine, P. V., Bunkóczi, G., Chen, V.B., Davis, I.W., Echols, N., Headd, J.J., Hung, L.-W., Kapral, G.J., Grosse-Kunstleve, R.W., McCoy, A.J., Moriarty, N.W., Oeffner, R., Read, R.J., Richardson, D.C., Richardson, J.S., Terwilliger, T.C., Zwart, P.H., IUCr, 2010. *PHENIX* : a comprehensive Python-based system for macromolecular structure solution. Acta Crystallogr. Sect. D Biol. Crystallogr. 66, 213–221. https://doi.org/10.1107/S0907444909052925

An, Y.J., Rowland, S.E., Na, J.-H., Spigolon, D., Hong, S.K., Yoon, Y.J., Lee, J.-H., Robb, F.T., Cha, S.-S., 2017. Structural and mechanistic characterization of an archaeal-like chaperonin from a thermophilic bacterium. Nat. Commun. 8, 827. https://doi.org/10.1038/s41467-017-00980-z

Bigotti, M.G., Clarke, A.R., 2008. Chaperonins: The hunt for the Group II mechanism. Arch. Biochem. Biophys. 474, 331–339. https://doi.org/10.1016/J.ABB.2008.03.015

Chaston, J.J., Smits, C., Aragão, D., Wong, A.S.W., Ahsan, B., Sandin, S., Molugu, Sudheer K., Molugu, Sanjay K., Bernal, R.A., Stock, D., Stewart, A.G., 2016. Structural and Functional Insights into the Evolution and Stress Adaptation of Type II Chaperonins. Structure 24, 364–374. https://doi.org/10.1016/J.STR.2015.12.016

Chaudhry, C., Horwich, A.L., Brunger, A.T., Adams, P.D., 2004. Exploring the Structural Dynamics of the E. coli Chaperonin GroEL Using Translation-libration-screw Crystallographic Refinement of Intermediate States. J. Mol. Biol. 342, 229–245. https://doi.org/10.1016/J.JMB.2004.07.015

Chen, J., Yagi, H., Furutani, Y., Nakamura, T., Inaguma, A., Guo, H., Kong, Y., Goto, Y., 2015. Self-assembly of the chaperonin GroEL nanocage induced at submicellar detergent. Sci. Rep. 4, 5614. https://doi.org/10.1038/srep05614

Croll, T.I., 2018. *ISOLDE* : a physically realistic environment for model building into low-resolution electron-density maps. Acta Crystallogr. Sect. D Struct. Biol. 74, 519–530. https://doi.org/10.1107/S2059798318002425

Emsley, P., Lohkamp, B., Scott, W.G., Cowtan, K., IUCr, 2010. Features and development of *Coot*. Acta Crystallogr. Sect. D Biol. Crystallogr. 66, 486–501. https://doi.org/10.1107/S0907444910007493

Furutani, M., Iida, T., Yoshida, T., Maruyama, T., 1998. Group II chaperonin in a thermophilic methanogen, Methanococcus thermolithotrophicus. Chaperone activity and filament-forming ability. J. Biol. Chem. 273, 28399–407. https://doi.org/10.1074/jbc.273.43.28399

Goddard, T.D., Huang, C.C., Meng, E.C., Pettersen, E.F., Couch, G.S., Morris, J.H., Ferrin, T.E., 2018. UCSF ChimeraX: Meeting modern challenges in visualization and analysis. Protein Sci. 27, 14–25. https://doi.org/10.1002/pro.3235

Jonuscheit, M., Martusewitsch, E., Stedman, K.M., Schleper, C., 2003. A reporter gene system for the hyperthermophilic archaeon Sulfolobus solfataricus based on a selectable and integrative shuttle vector. Mol. Microbiol. 48, 1241–1252. https://doi.org/10.1046/j.1365-2958.2003.03509.x

Kagawa, H.K., Yaoi, T., Brocchieri, L., McMillan, R.A., Alton, T., Trent, J.D., 2003. The composition, structure and stability of a group II chaperonin are temperature regulated in a hyperthermophilic archaeon. Mol. Microbiol. 48, 143–156. https://doi.org/10.1046/j.1365-2958.2003.03418.x

Li, Y., Paavola, C.D., Kagawa, H., Chan, S.L., Trent, J.D., 2007. Mutant chaperonin proteins: new tools for nanotechnology. Nanotechnology 18, 455101. https://doi.org/10.1088/0957-4484/18/45/455101

Lin, Z., Puchalla, J., Shoup, D., Rye, H.S., 2013. Repetitive protein unfolding by the trans ring of the GroEL-GroES chaperonin complex stimulates folding. J. Biol. Chem. 288, 30944–55. https://doi.org/10.1074/jbc.M113.480178

Lopez, T., Dalton, K., Frydman, J., 2015. The Mechanism and Function of Group II Chaperonins. J. Mol. Biol. 427, 2919–2930. https://doi.org/10.1016/j.jmb.2015.04.013

Muñoz, I.G., Yébenes, H., Zhou, M., Mesa, P., Serna, M., Park, A.Y., Bragado-Nilsson, E., Beloso, A., de Cárcer, G., Malumbres, M., Robinson, C. V, Valpuesta, J.M., Montoya, G., 2011. Crystal structure of the open conformation of the mammalian chaperonin CCT in complex with tubulin. Nat. Struct. Mol. Biol. 18, 14–19. https://doi.org/10.1038/nsmb.1971

Pettersen, E.F., Goddard, T.D., Huang, C.C., Couch, G.S., Greenblatt, D.M., Meng, E.C., Ferrin, T.E., 2004. UCSF Chimera - A visualization system for exploratory research and analysis. J. Comput. Chem. 25, 1605–1612. https://doi.org/10.1002/jcc.20084

Pintilie, G.D., Zhang, J., Goddard, T.D., Chiu, W., Gossard, D.C., 2010. Quantitative analysis of cryo-EM density map segmentation by watershed and scale-space filtering, and fitting of structures by alignment to regions. J. Struct. Biol. 170, 427–438. https://doi.org/10.1016/J.JSB.2010.03.007

Punjani, A., Rubinstein, J.L., Fleet, D.J., Brubaker, M.A., 2017. cryoSPARC: algorithms for rapid unsupervised cryo-EM structure determination. Nat. Methods 14, 290–296. https://doi.org/10.1038/nmeth.4169

Quehenberger, J., Shen, L., Albers, S.-V., Siebers, B., Spadiut, O., 2017. Sulfolobus - A Potential Key Organism in Future Biotechnology. Front. Microbiol. 8, 2474. https://doi.org/10.3389/fmicb.2017.02474

Rohou, A., Grigorieff, N., 2015. CTFFIND4: Fast and accurate defocus estimation from electron micrographs. J. Struct. Biol. 192, 216–221. https://doi.org/10.1016/J.JSB.2015.08.008

Saibil, H., 2013. Chaperone machines for protein folding, unfolding and disaggregation. Nat. Rev. Mol. Cell Biol. 14, 630–642. https://doi.org/10.1038/nrm3658

Saibil, H.R., Fenton, W.A., Clare, D.K., Horwich, A.L., 2013. Structure and Allostery of the Chaperonin GroEL. J. Mol. Biol. 425, 1476–1487. https://doi.org/10.1016/J.JMB.2012.11.028

Skjærven, L., Cuellar, J., Martinez, A., Valpuesta, J.M., 2015. Dynamics, flexibility, and allostery in molecular chaperonins. FEBS Lett. 589, 2522–2532. https://doi.org/10.1016/J.FEBSLET.2015.06.019

Tang, G., Peng, L., Baldwin, P.R., Mann, D.S., Jiang, W., Rees, I., Ludtke, S.J., 2007. EMAN2: An extensible image processing suite for electron microscopy. J. Struct. Biol. 157, 38–46.

https://doi.org/10.1016/J.JSB.2006.05.009

Trabuco, L.G., Villa, E., Mitra, K., Frank, J., Schulten, K., 2008. Flexible Fitting of Atomic Structures into Electron Microscopy Maps Using Molecular Dynamics. Structure 16, 673–683. https://doi.org/10.1016/J.STR.2008.03.005

Trent, J.D., Kagawa, H.K., Yaoi, T., 1998. The role of chaperonins in vivo: The next frontier. Ann. N. Y. Acad. Sci. 851, 36–47. https://doi.org/10.1111/j.1749-6632.1998.tb08974.x

Trent, J.D., Kagawa, H.K., Yaoi, T., Olle, E., Zaluzec, N.J., 1997. Chaperonin filaments: The archaeal cytoskeleton? Proc. Natl. Acad. Sci. 94, 5383–5388. https://doi.org/10.1073/PNAS.94.10.5383

Trent, J.D., Nimmesgern, E., Wall, J.S., Hartl, F.-U., Horwich, A.L., 1991. A molecular chaperone from a thermophilic archaebacterium is related to the eukaryotic protein t-complex polypeptide-1. Nature 354, 490–493. https://doi.org/10.1038/354490a0

Trent, J.D., Osipiuk, J., Pinkau, T., 1990. Acquired thermotolerance and heat shock in the extremely thermophilic archaebacterium Sulfolobus sp. strain B12. J. Bacteriol. 172, 1478–84. https://doi.org/10.1128/jb.172.3.1478-1484.1990

Weiss, C., Jebara, F., Nisemblat, S., Azem, A., 2016. Dynamic Complexes in the Chaperonin-Mediated Protein Folding Cycle. Front. Mol. Biosci. 3, 80. https://doi.org/10.3389/fmolb.2016.00080

Whitelam, S., Rogers, C., Pasqua, A., Paavola, C., Trent, J., Geissler, P.L., 2009. The Impact of Conformational Fluctuations on Self-Assembly: Cooperative Aggregation of Archaeal Chaperonin Proteins. Nano Lett. 9, 292–297. https://doi.org/10.1021/nl8029306

Zang, Y., Jin, M., Wang, H., Cui, Z., Kong, L., Liu, C., Cong, Y., 2016. Staggered ATP binding mechanism of eukaryotic chaperonin TRiC (CCT) revealed through high-resolution cryo-EM. Nat. Struct. Mol. Biol. 23, 1083–1091. https://doi.org/10.1038/nsmb.3309

Zheng, S.Q., Palovcak, E., Armache, J.-P., Verba, K.A., Cheng, Y., Agard, D.A., 2017. MotionCor2: anisotropic correction of beam-induced motion for improved cryo-electron microscopy. Nat. Methods 14, 331–332. https://doi.org/10.1038/nmeth.4193

Zivanov, J., Nakane, T., Forsberg, B.O., Kimanius, D., Hagen, W.J., Lindahl, E., Scheres, S.H., 2018. New tools for automated high-resolution cryo-EM structure determination in RELION-3. Elife 7. https://doi.org/10.7554/eLife.42166